Laser writing of coherent colour centres in diamond

Supplementary Information

Yu-Chen Chen[1], Patrick S. Salter[2], Sebastian Knauer[3], Laiyi Weng[1], Angelo C. Frangeskou[4], Colin J. Stephen[4], Shazeaa N. Ishmael[4], Philip R. Dolan[1], Sam Johnson[1], Ben L. Green[4], Gavin W. Morley[4], Mark E. Newton[4], John G. Rarity[3], Martin J. Booth[2] and Jason M. Smith[1,*]

[1] Department of Materials, University of Oxford, Parks Road, Oxford OX1 3PH, UK

[2] Department of Engineering Science, University of Oxford, Parks Road, Oxford OX1 3PJ, UK

[3] Department of Electronics and Electrical Engineering, University of Bristol, Merchant Venturers Building, Woodland Road, Bristol, BS8 1UB, UK

[4] Department of Physics, University of Warwick, Coventry, CV4 7AL, UK

Samples

The paper contains data recorded from two nominally identical samples, labelled A and B, both of which were commercial 'electronic grade' single crystal plates from Element Six as described in the Methods section, which were processed in an identical manner. The PL images and spectra in figure 1, NV population data in figures 2a-e, and spin coherence data in figure 4 were recorded from sample A. NV positioning data in figure 2f and raw PLE data in figure 3

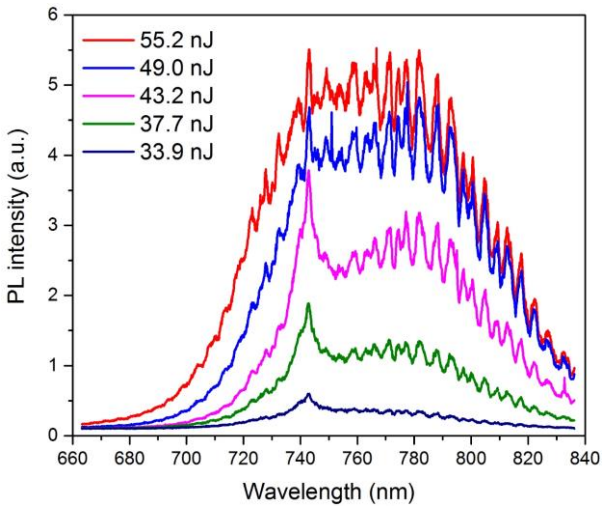

Figure S1 | Fluorescence spectra from laser processed sites (pre-anneal) at different pump pulse energies (sample A).

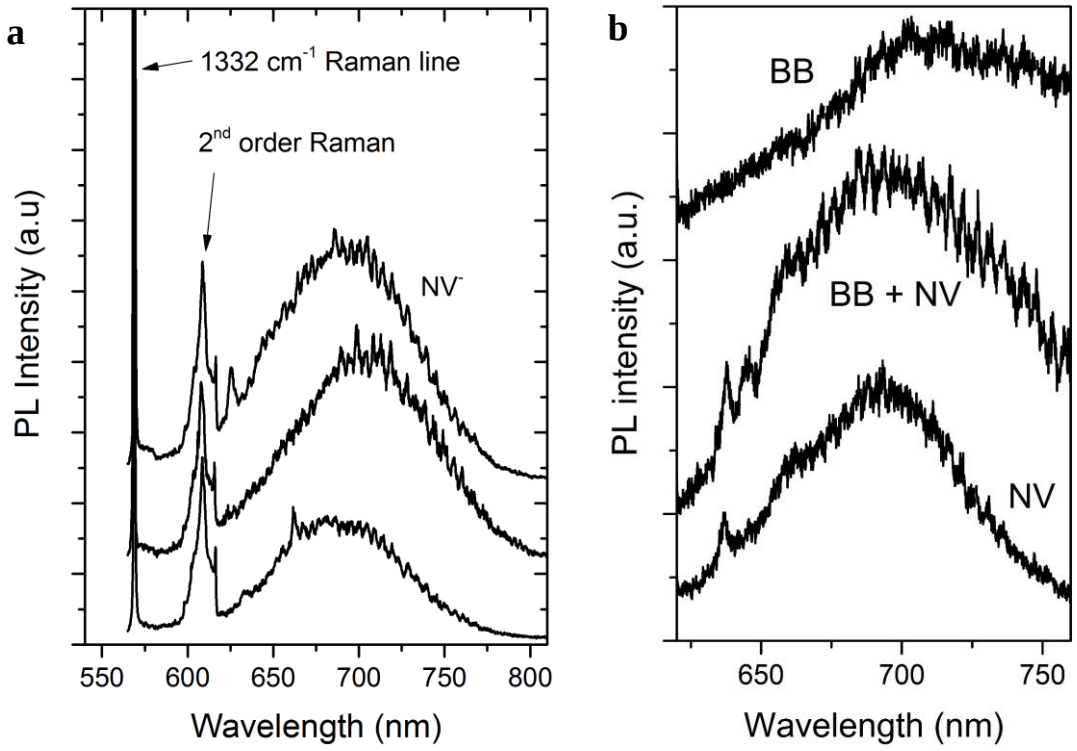

Figure S2 | Additional PL spectra recorded from post-annealed samples. **a** Spectra from region $E_p < E_2$ showing Raman and NV- signals with no evidence of NV^0 emission (ZPL at 575 nm). **b** Spectra from sites with $E_p > E_2$. Broad-band (BB) emission is observed (top plot), and spectra in which BB and NV emission are both present (middle plot). The spectra are offset in the vertical direction for clarity.

were recorded from sample B. PLE line widths from both samples are displayed in figure 3d. Spin coherence measurements were performed on NV centres in both samples, with no significant difference in the results.

Sample B showed about half the probability of generating NV centres compared with sample A for the same laser pulse energy. We attribute this reduced NV generation rate to a lower nitrogen concentration (the nitrogen concentrations in both samples are below the limit at which bulk electron Paramagnetic Resonance measurements can measure them.)

Additional PL spectra of laser processed sites

Fluorescence spectra were recorded from multiple sites in sample A prior to annealing (main text figure 1a). Figure S1 shows recorded spectra as a function of the laser writing pulse energy. These spectra reveal that the GR1 peak at 740 nm is visible for $E_p > 30$ nJ but at higher pulse energies becomes swamped by a broad signal at longer wavelengths originating from extended defects. The rapid modulation in the signal for wavelengths above 750 nm is due to an etaloning effect in the CCD camera.

Figure S2 shows additional typical fluorescence spectra recorded from the post-annealed samples. For $E_p < E_2$ (plot a) only NV^- emission is observed, with GR1 and NV0 both absent. For $E_p > E_2$ (plot b) NV^- emission is seen along with additional broad-band fluorescence suggestive of a high density of extended defects remaining in the material. Wherever combined NV^- and BB fluorescence was observed the photon autocorrelation dip was found to be significantly suppressed. We note that no significant fluorescence from the neutral nitrogen-vacancy centre, NV^0, was detected at any writing pulse energy below E_2, suggesting that a low density of vacancies and other electron traps exists after the anneal.

Time-resolved Photoluminescence of NV3 in Sample B

The excited state lifetime NV3 in sample B (one of the defects showing a narrow PLE line width at a temperature of 4.2 K) was measured directly from the time-resolved photoluminescence decay (TRPL) using the time-correlated single photon counting (TCSPC) technique. Excitation was with a 532 nm frequency-doubled diode-pumped-solid-state laser with 50 ps pulse durations (PicoQuant LDH-FA), and detection with an Excelitas SPCM AQR-14 single photon counting detector. Timing was recorded with an Edinburgh Instruments TCC900 PCI card. The decay function was recorded by measuring the TCSPC signal when focused on the NV defect then substracting the TCSPC signal from a nearby region of bare diamond. The instrumental response function was also measured by removing the laser blocking filter and inserting a neutral density filter to measure attenuated reflection of the laser. The instrumental response function was then convoluted with a single exponential decay and fitted to the NV centre decay function, with a lifetime T_1 and amplitude introduced as fitting parameters. Figure S3 shows a plot of the decay function after background removal, and the best fit to the data for a single exponential decay of lifetime T_1 convoluted with the instrumental response.

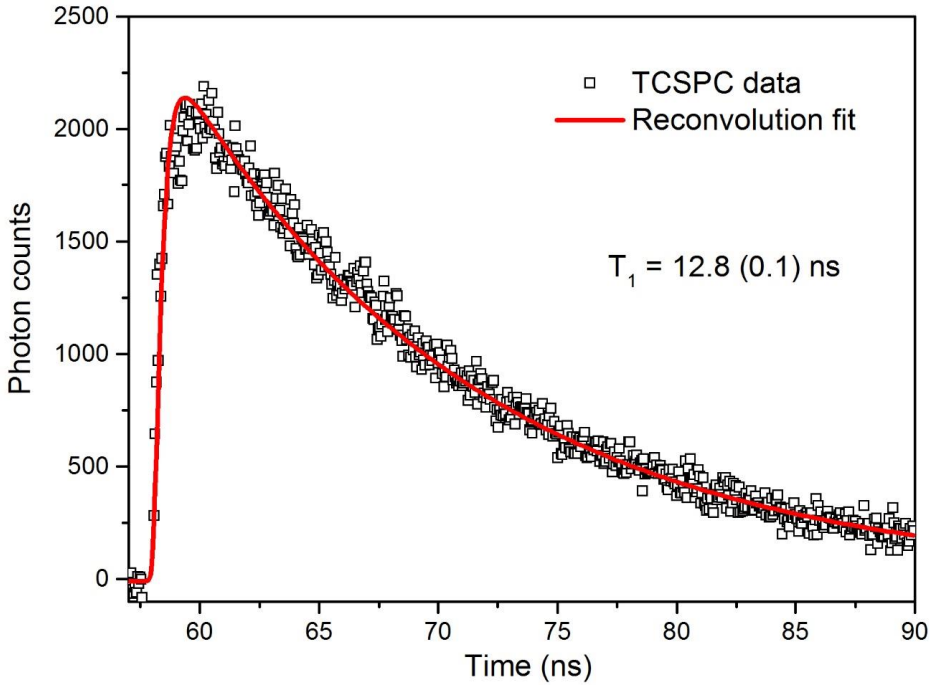

Figure S3 | Time-resolved photoluminescence of NV3 in sample B at 4.2K, fitted with a single exponential decay convoluted with the instrumental response of the TCSPC apparatus.

Laser writing of vacancies

The optical layout for the laser writing is shown in Figure S4a.

The use of high numerical aperture focussing is necessary to limit the size of the laser focus, and move into a regime appropriate for the generation of single localised NVs as opposed to NV ensembles that tend to form around regions of laser-induced graphitisation [Pimenov]. However, using high NA optics to focus beneath the surface of diamond introduces significant amounts of spherical aberration, due to refraction at the oil/diamond interface where there is a large step in refractive index. It is necessary to correct the aberration to restore optimum optical performance, which has also been shown to enhance the light matter interaction when laser writing sub-surface graphitic tracks [Sun]. The effect of the aberration correction is to provide dramatic reduction in size of the laser focus (Fig 1b). Since the spherical aberration at the diamond/oil interface is the dominant aberration source, the correction produces a particularly marked improvement in the axial (z) direction. We have shown previously that the use of

adaptive optics enables accurate laser fabrication in diamond to depths of at least 220 µm [Simmonds].

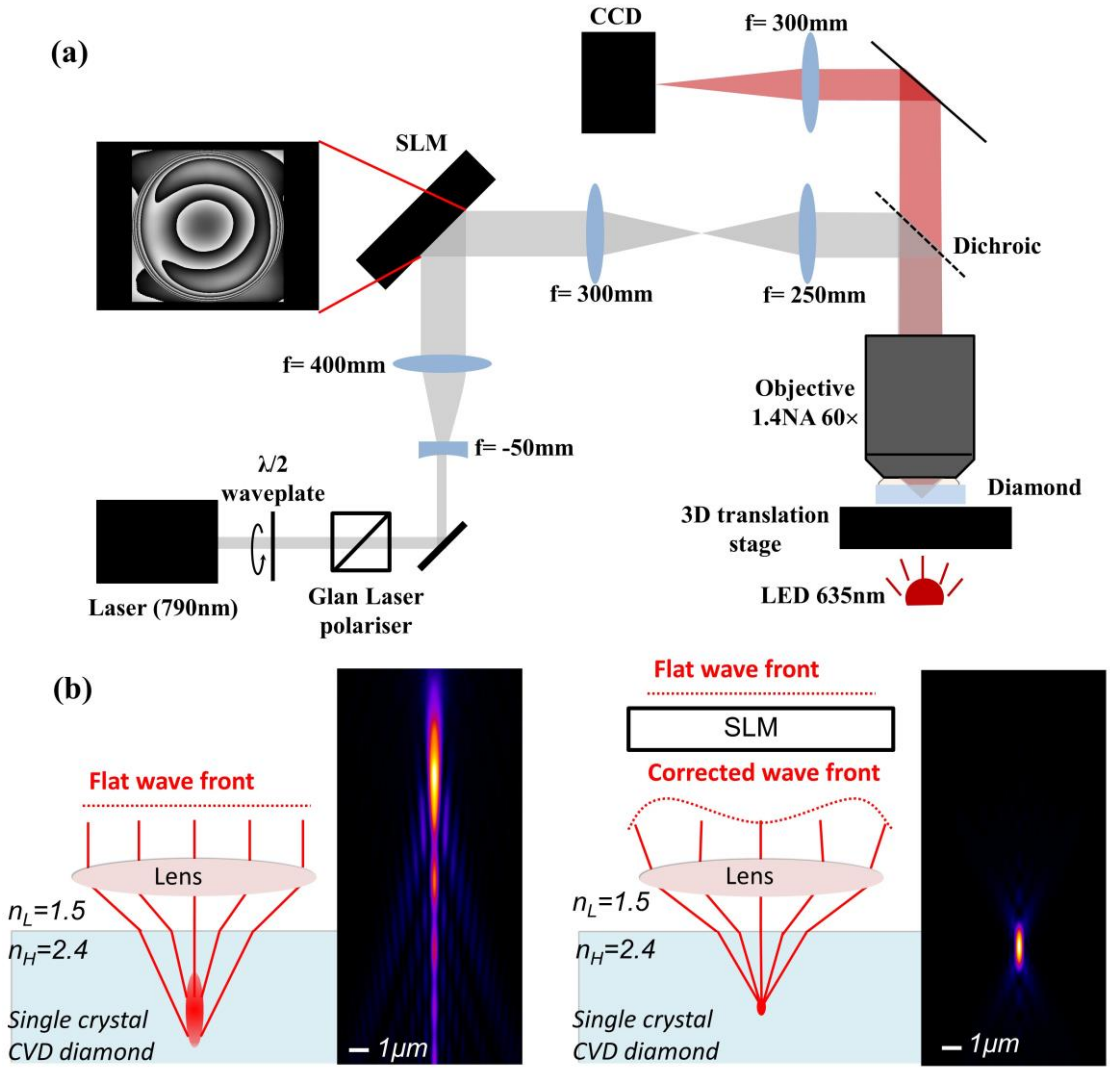

Figure S4 | Aberration-corrected laser writing. **a**, Schematic of laser processing apparatus. The phase pattern displayed on the SLM compensated optical aberrations in the system and those introduced by focussing into the diamond. **b**, The effect of aberration correction on the laser focal intensity distribution when focused through the planar oil/diamond interface to a depth of 50 µm. Without correction the focus is drastically elongated in z by spherical aberrations. With aberration correction good z resolution is achieved.

The focal spot of the laser in the diamond is expected to be close to the diffraction-limit, with transverse and axial dimensions (full width half maximum) of 350 nm and 1.7 µm respectively, giving a focal volume of around 0.16 μm^3. However, the volume over which the vacancies are generated is expected to be considerably smaller, since the interaction of the pulse with the

diamond is highly non-linear [Lagomarsino]. At high pulse energies there is expected to be a distinct threshold for optical breakdown which may be exploited [Joglekar, Juodkazis].

Pulse energy control

The laser pulse energy was precisely controlled using a rotatable half waveplate before a Glan-

Angle of λ/2 waveplate (degrees)	Pulse energy before objective (nJ)	Pulse energy (nJ) after objective
5	118.0	82.6
30µm gap		
3.6	61.8	43.2
3.4	55.2	38.6
3.2	49.0	34.3
3	43.2	30.2
2.8	37.7	26.4
2.75	36.4	25.5
2.7	35.1	24.6
2.65	33.9	23.7
2.6	32.6	22.8
2.55	31.4	22.0
2.5	30.2	21.1
2.45	29.0	20.3
2.4	27.9	19.5
2.35	26.8	18.7
2.3	25.7	18.0
2.25	24.6	17.2
2.2	23.6	16.5
2.15	22.5	15.8
2.1	21.5	15.1
2.05	20.5	14.4
2	19.6	13.7
1.95	18.7	13.1
1.9	17.7	12.4
1.85	16.9	11.8
1.8	16.0	11.2

Table S1 Laser pulse energies used for the writing of vacancies in sample A. The energies measured before the objective are the ones quoted in the main text.

Laser polariser. Pulse energies for the 25 waveplate settings used for fabrication of the array in sample A are shown in table S1 below. Pulse energy measurements (2nd column) were taken immediately before the objective. The final column gives the pulse energy reduced by a factor of 0.7 due to the transmission loss of the objective lens, based on the manufacturer‘s

specifications. For the pulse energy at the focus, one must also take into account Fresnel reflection at the diamond interface which can be significant due to the large angles involved. The first row of the fabrication grid was at sufficient pulse energy (118 nJ) for considerable graphitisation and could hence be seen using a standard transmission microscope. These were used as location markers since the rest of the fabrication array produced too little structural modification within the diamond to be seen by standard widefield microscopy methods and were only revealed via their photoluminesence.

Vacancy generation in diamond

Identification of the mechanism responsible for GR1 generation is important in order to determine the potential of laser writing for accurate positioning of NV centres, which will ultimately be limited by the accuracy of vacancy generation.

Laser writing creates defects in the lattice via the generation of energetic seed electrons by multi-photon ionisation (MPI), and tunneling (Zener) breakdown, combined with impact ionisation and heat dissipation [3]. The dominant mechanism for seed generation is typically delineated by the Keldysh parameter

$$\gamma = \frac{\omega}{e}\sqrt{\frac{mcn\varepsilon_0 E_g}{I}}$$

where ω and I are the laser frequency and intensity, while m, c, n, ε_0 and E_g are the electron effective mass, speed of light in vacuum, linear refractive index, permittivity of free space, and the direct band gap respectively. MPI is dominant over tunneling breakdown for $\gamma > 1$ corresponding to

$$I < \frac{mcn\varepsilon_0 E_g \omega^2}{e^2}.$$

For the parameters used here ($m = 0.4m_e, n = 2.4, E_g = 7.1$ eV, and $\omega = 2.4 \times 10^{15}$s^{-1}) assuming a pulse duration of 300 fs and a beam waist of 350 nm, and allowing for Fresnel reflection at the oil/diamond interface and losses in the objective, the equation above predicts that MPI will dominate for pulse energies below about 25 nJ.

The recent work Lagomarsino *et al*. [24] concludes that in the MPI regime, carrier densities of order 10^{16} cm^{-3} sufficient to induce lattice damage result from illumination intensities between 1-10 TW cm^{-2}, and occur via a 9-photon absorption process. This intensity range compares well with that for the focused laser spot in our experiments.

We note that since the lattice damage is created by the heat generated subsequent to photoionisation, there is no direct link between the degree of nonlinearity and the energy needed to dislodge an atom from the lattice. Each photon in the λ = 790 nm laser pulse carries an energy of 1.57 eV, suggesting that energy is transferred to the diamond in packets of 14 eV, whereas the displacement threshold energy is thought to fall in the region of 35-40 eV [Koike, Delgado].

Annealing

Four different annealing recipes were tried: 3 hours at at 900 degrees Celsius, 3 hours at 1000 degrees Celsius, 24 hours at 1200 degrees Celsius, and a multi-step process following Chu et al [21] involving 4 hours at 400 degrees Celsius, 2 hours at 800 degrees Celsius and 2 hours at 1200 degrees Celsius, with 3 degrees Celsius / minute ramping rate between steps.

The sample annealed at 900 degrees we observed that a few NV^- centres were generated on the original damage position, but that most of the GR1 defects and other damage remained. This result is consistent with literature reports that most extended vacancy defects created by implantation process are destroyed at temperatures above about 1000 degrees Celsius as reported in reference [26] of the main text. The 1000 degrees anneal produced many single NV^- defects as reported in the main text. Subsequent annealing of the same sample at 1200 degrees Celsius for 24 hours resulted in no new NV^- centres, and all the generated NV^- centres in previous array disappeared. No NV^- centre was generated after the multi-step process annealing from reference [21] in the main text. We concluded that a 3 hours 1000 degrees Celsius annealing was the optimal condition for this laser fabrication method.

During annealing, the vacancies are expected to diffuse an average distance $\sqrt{Dt}$ where D is the diffusivity and t is the anneal time. For an initial vacancy distribution that is point-like in the x-y plane and infinite in the z direction, isotropic diffusion yields a cylindrically symmetric vacancy distribution after annealing, following

$$n_V(r) = Are^{-r^2/4Dt} \tag{1}$$

The fit shown in figure 2f of the Letter therefore provides $\sqrt{Dt} = r_0/2 = 98 \pm 1$ nm, giving a value of $D = 3.7 \times 10^{-14}$ cm^2 s^{-1}. Diffusion of vacancies in diamond is a thermally activated hopping process the activation energy for which can be expressed as

$$\Delta = -kTln\left(\frac{D}{D_0}\right), \tag{2}$$

where kT is the thermal energy. Using $D_0 = 3.6 \times 10^{-6}$ cm^2 s^{-1} [Hu] we find that $\Delta = 2.0$ eV, consistent with values presented in other reports [Bernholc, Mainwood, Orwa].

Characterisation of residual stress

To investigate whether the laser writing and annealing treatment had resulted in residual stress in the diamond sample we imaged the optical birefringence and the Raman scattering signal of sample B. Figure S6 shows a greyscale optical birefringence image recorded by placing the sample between orthogonal linear polarisers and measuring the transmitted broadband light. On the right hand side of the image two test rows created with writing pulse energies in excess of 100 nJ are clearly observed. Towards the centre of the image, three rows from the main array are visible, corresponding to the highest writing pulse energies of 60 – 75 nJ. No birefringence is visible at the sites processed with lower laser pulse energies.

To extract quantitative information on residual stress we performed Raman mapping of the same sample (figure S7). To produce the map, Raman spectra of the first order peak at 1332 cm^{-1} were obtained using 532 nm excitation and dispersed with a 2400 lines / mm grating. The peaks were fitted with the pseudo-Voigt line shape

$$y(x) = A\left((1-\eta)\exp\left(-\ln(2)\frac{x-x_0}{\sigma}\right) + \frac{\eta}{1+\left(\frac{x-x_0}{\sigma}\right)^2}\right) + c$$

with Lorentzian-Gaussian character η, peak position x_0 and linewidth σ. Figure S7 a, c, and d show maps of the peak width, position, and height, and plot b shows three of the fitted peaks corresponding to positions on the sample identified in plot a.

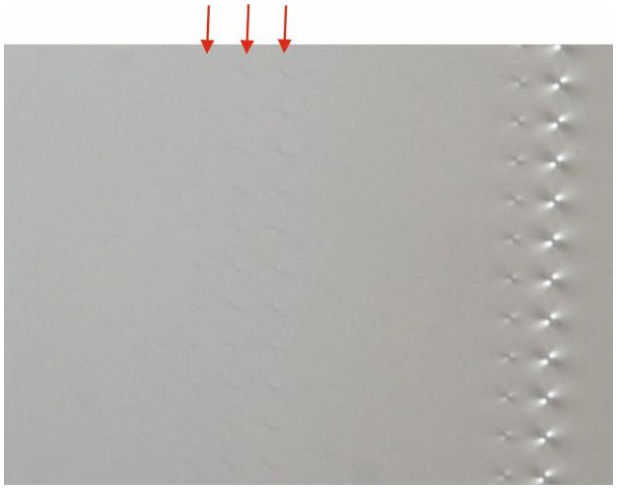

Figure S6 | Birefringence image of sample B measured using orthogonal linear polarisers. Red arrows indicate the locations of the rows of features created by the three highest writing pulse energies (60 – 75 nJ) in the main array.

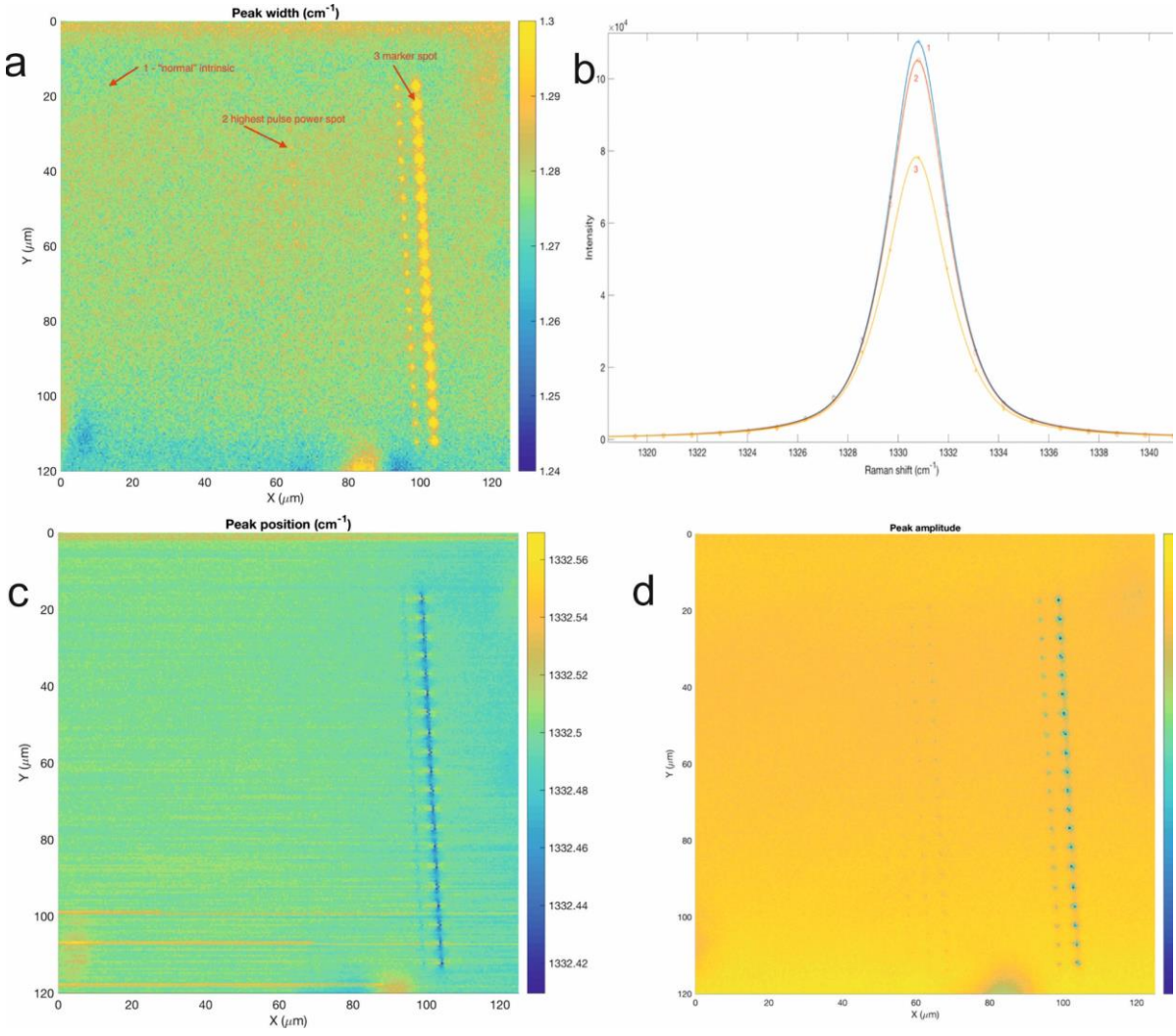

Figure S7 | Raman maps of sample B. (a) Colour-scale map of the width of the first order Raman peak. (b) Example fits of the pseudo-Voigt function for the three points labelled in plot (a). (c) and (d) are maps of the Raman peak position and peak amplitude obtained from the fits.

The 1332 cm^{-1} peak position appears to be relatively insensitive to the laser processing, with only the two rows of calibration markers visible in figure S7c. Small changes in the peak width and height can on the other hand be observed for the first three highest energy rows of the main array. The measured changes in peak width provide a means to estimate the residual stress. We make the conservative assumption that the measured change in width is due to stress along the crystal with the smallest-splitting coefficient ([001], upper bound) for which which $\Delta\omega = 0.73 \pm 0.1$ cm^{-1} / GPa. The observed increase in width of about 0.01 cm^{-1} for pulse energies of 60 – 75 nJ therefore suggests residual stress of around 14 MPa. This places a conservative upper limit on the residual stress generated at the pulse energies of 20 nJ and below, which, based on the observed change in fluorescence intensity from the laser processed sites in figure S5, could be two orders of magnitude smaller.

Photoluminescence measurements of positioning accuracy

The full design and specifications of the custom-built scanning confocal microscope used for the experiments are reported in reference [Grazioso].

Positioning accuracy in the image plane was determined by fitting a 2D Gaussian to the PL intensity distribution of each colour centre as described in the Methods section. Figure S8 shows

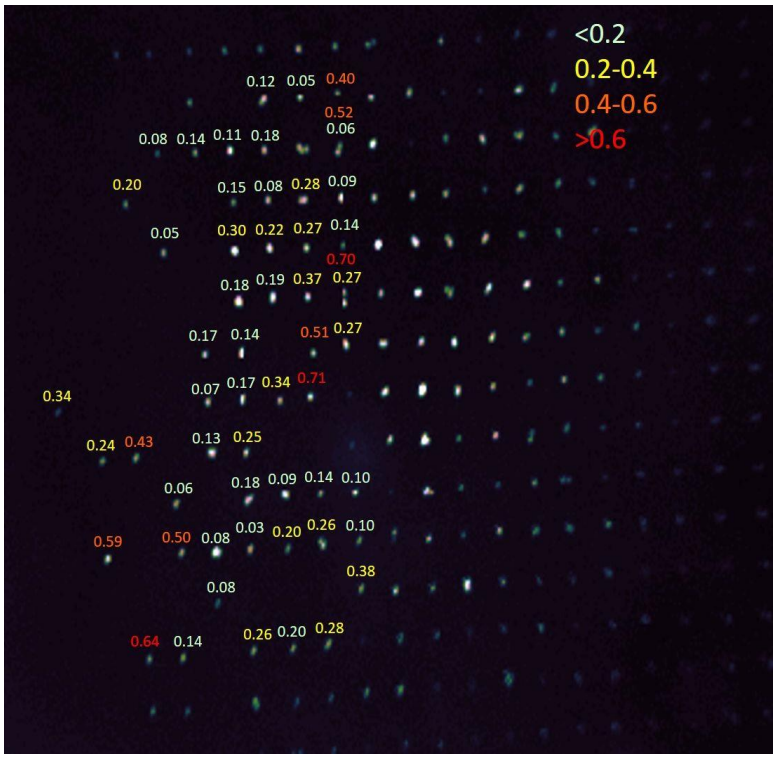

Figure S8 | Positioning accuracy of NV generation in sample B. Labels show the displacement of NV centres from their respective grid positions (in micrometres), after removal of a quadratic field distortion. The labels are colour-coded into four magnitude groups to reveal any systematic trends that would indicate further uncompensated field distortion.

a map of the resultant displacements for sample B. That there is little evidence of systematic order in the displacements suggests that the major field distortions have been corrected, and that the remaining displacements therefore reflect the random location of the NV centres about the target sites. For sample A it was not possible to remove the field distortion in this manner, and so an equivalent map is not presented.

Spin resonance measurements

Figure S9 shows the laser and microwave pulse sequence for the Hahn echo measurements.

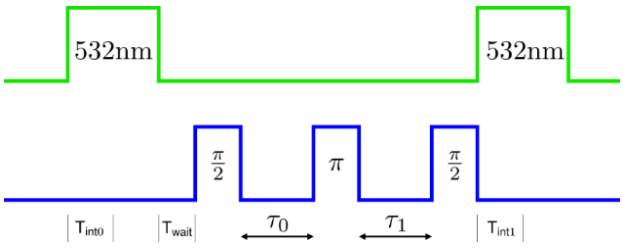

Figure S9 | Pulse sequence for the Hahn echo measurements. Laser gating is indicated in green and microwave gating in blue.

.

References

[Bernholc] Bernholc, J., Antonelli, A., Del Sole, T. M., Bar-Yam, Y., & Pantelides, S. T., Mechanism of self-diffusion in diamond, Phys. Rev. Lett. **61**, 2689 (1988).

[Delgado] Delgado, D. and Vila, R., Statistical Molecular Dynamics study of displacement energies in diamond, J. Nuc. Mat. **419**, 32 (2011).

[Grazioso] Grazioso, F., Patton, B. R., & Smith, J. M., A high stability beam-scanning confocal optical microscope for low temperature operation, Rev. Sci. Inst. **81**, 093705 (2010).

[Hu] Hu, X. J. *et al.*, The diffusion of vacancies near a diamond (001) surface, Solid State Commun. **122**, 45 **(**2002).

[Joglekar] Joglekar, A. P., Liu, H. H., Meylhöfer, E., Mourou, G., & Hunt, A. J., Optics at critical intensity: applications to nanomorphing, Proc. Nat. Acad. Sci. **101**, 5856 (2004).

[Juodkazis] Juodkazis, S. *et al.*, Laser-induced microexplosion confined in the bulk of a sapphire crystal: evidence of multimegabar pressures, Phys. Rev. Lett. **96**, 166101 (2006).

[Koike] Koike, J., Parkin, D. M. and Mitchell, T. E., Displacement threshold energy for type IIa diamond, Appl. Phys. Lett. 60, 1450 (1992).

[Kurtsiefer] Kurtsiefer, C., Mayer, S., Zarda, P., & Weinfurter, H., A stable solid-state source of single photons, Phys. Rev. Lett. **85**, 290 (2000).

[Lagomarsino] Lagomarsino, S. *et al*., Photoionization of monocrystalline CVD diamond irradiated with ultrashort intense laser pulse, Phys. Rev. B **93**, 085128 (2016).

[Mainwood] Mainwood, A., Point defects in natural and synthetic diamond: what they can tell us about CVD diamond, Phys. Status Solidi (a) **172**, 25 (1999).

[Orwa] Orwa, J. O., Nugent, K. W. , Jamieson, D. N., & Prawer, S., Raman investigation of damage caused by deep ion implantation in diamond, Phys. Rev. B. **62**, 5461 (2000).

[Pimenov] Pimenov, S. M., Khomich, A. A., Neuenschwander, B., Jaggi, B. & Romano, V, Picosecond-laser bulk modification induced enhancement of nitrogen-vacancy luminescence in diamond, J. Opt. Soc. America B **33**, B49 (2016).

[Sun] Sun, B., Salter, P. S., & Booth, M. J., High conductivity micro-wires in diamond following arbitrary paths, Appl. Phys. Lett. **105**, 231105 (2014).